Nanoscale

ROYAL SOCIETY OF CHEMISTRY

PAPER

View Article Online
View Journal | View Issue

Cite this: *Nanoscale*, 2021, **13**, 12271

Carrier extraction from metallic perovskite oxide nanoparticles†

Calum McDonald, *[a,b] Chengsheng Ni, [c] Vladimir Švrček, [b] Manuel Macias-Montero, [a] Tamilselvan Velusamy, [a] Paul A. Connor, [c] Paul Maguire, [a] John T. S. Irvine [c] and Davide Mariotti [a]

Received 6th May 2021,
Accepted 14th June 2021

DOI: 10.1039/d1nr02890a

rsc.li/nanoscale

We observe the extraction of carriers excited between two types of bands in the perovskite oxide, Sr-deficient strontium niobate ($Sr_{0.9}NbO_3$). $Sr_{0.9}NbO_3$ exhibits metallic behaviour and high conductivity, whilst also displaying broad absorption across the ultraviolet, visible, and near-infrared spectral regions, making it an attractive material for solar energy conversion. Furthermore, the optoelectronic properties of strontium niobate can easily be tuned by varying the Sr fraction or through doping. Sr-deficient strontium niobate exhibits a split conduction band, which enables two types of optical transitions: intraband and interband. However, whether such carriers can be extracted from an unusual material as such remains unproven. In this report, we have overcome the immense challenge of photocarrier extraction by fabricating an extremely thin absorber layer of $Sr_{0.9}NbO_3$ nanoparticles. These findings open up great opportunities to harvest a very broad solar spectral absorption range with reduced recombination losses.

1. Introduction

With continuous density of states extending above the Fermi level that enables the absorption of a broad range of frequencies of light, metallic conductors are attractive for utilising solar energy in numerous applications.[1–4] However, the challenge associated with metallic conductors lies in the separation and extraction of photoexcited charge carriers with lifetimes that are usually very short (~1 ps).[5] The possibility of maintaining given metallic features in a modified energy band structure that allows improved extraction is therefore highly desirable. Materials such as perovskite oxides (ABO_3) can be designed to possess unique electronic structures that could offer advantages over materials with standard metallic behaviour, whilst their characteristic density of states results in strong absorption of light across a broad range of the visible spectrum, presenting significant opportunities for solar energy conversion.[3,4]

Perovskite oxides and their derivatives (layered perovskite oxides) represent a large family of materials which exhibit a multitude of properties and have been investigated for applications in ferromagnetism,[6] ferroelectrics,[7,8] dielectrics,[9] photovoltaics,[10,11] superconductors,[12] photocatalysts,[13,14] plasmonics,[15] electrocatalysts,[16] *etc*. Perovskite oxides possess a high-degree of flexibility given that 90% of the metallic elements in the periodic table can adopt a stable perovskite-type oxide structure.[17] Most semiconducting perovskite oxides have large bandgaps (~3–5 eV) due to oxygen-metal transitions and the large differences in their electronegativities,[10,18] and are therefore generally unsuitable for absorbing light within the solar spectral range. Interestingly, the metallic perovskite oxide strontium niobate ($SrNbO_3$), which displays broad visible light absorption along with an optical gap of approximately 1.8–2 eV,[2,19] has previously been demonstrated as a photocatalyst in its Sr-deficient forms (*e.g.* Sr_xNbO_3)[2,19] where the exact nature of its photocatalytic behaviour is not yet well understood. The properties of strontium niobate are generally attractive for use in solar energy conversion. It is highly stable against photocatalytic degradation[2] indicating that it should not degrade under illumination. The crystal structure, bandgap, conductivity, and photoactivity have been reported to be dependent on the fraction of Sr,:[20,21] *i.e.* strontium niobate has been demonstrated to be highly tunable, particularly through variations in the Sr deficiency. Previous studies on a series of Sr-deficient Sr_xNbO_3 demonstrated that x = 0.9 gives the highest photocatalytic activity, preferable bandgap, and highest carrier mobility.[19–21] Further details are provided in the ESI (Note 1).†

The band structure of strontium niobate is rather unique, giving rise to unique properties and opportunities,[2] and has

[a]*Nanotechnology & Integrated Bio-Engineering Centre (NIBEC), Ulster University, BT37 0QB, UK. E-mail: calum.mcdonald@aist.go.jp*
[b]*Global Zero-Emission Research Center, National Institute of Advanced Industrial Science and Technology (AIST), Central 2, Umezono 1-1-1, Tsukuba, 305-8568, Japan*
[c]*School of Chemistry, University of St Andrews, St Andrews, Fife, KY16 9ST, UK*
†Electronic supplementary information (ESI) available. See DOI: 10.1039/d1nr02890a

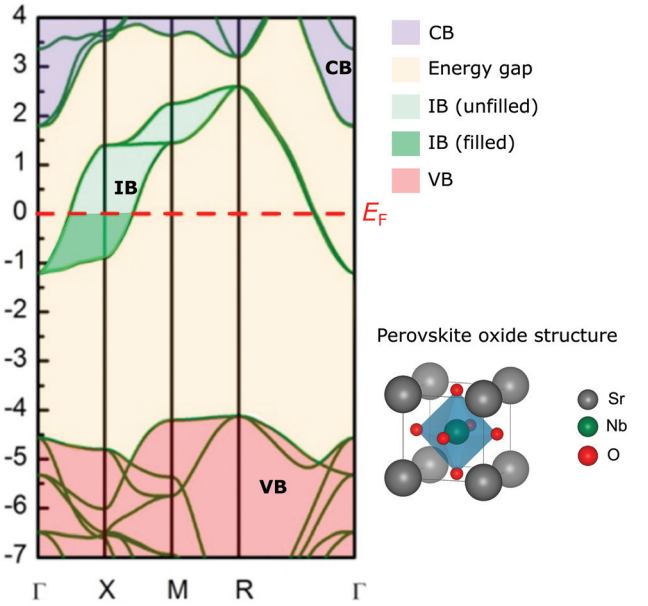

Fig. 1 Density functional theory for $SrNbO_3$ and the unit cell structure. CB, IB, VB, and E_F refer to the conduction band, intermediate band, valence band, and Fermi level, respectively. Adapted from Zhu *et al.* with permission, copyright [2013] American Chemical Society.[22]

been detailed by Zhu *et al.*[22] and an annotated version of their density functional theory (DFT) result is shown in Fig. 1. The Fermi level lies in an intermediate band comprised mostly of Nb 4d t_{2g} states, termed IB, which exists between the conduction band (CB) and the valence band (VB). The bottom of the CB consists of predominantly Sr 3d states, whilst the VB is of O 2p states as per usual for a metal oxide. Between the VB band and the IB there is an absence of available states which gives rise to an energy gap which is >4 eV. Therefore, transitions from the VB to an unoccupied state in the IB are possible, though with a relatively high minimum energy, which for instance would represent a very small proportion of the available solar spectrum.

From the IB to the CB there is an indirect gap of approximately 1.9 eV and a direct gap of approximately 2.4 eV. The unfilled IB states which extends above the Fermi level overlap with the bottom energy states of the CB but they are separated in *k*-space. The energy gap existing between the IB and the CB likely accounts for the strong onset of visible light absorption beginning from ~700 nm which then extends into the ultraviolet spectrum as previously reported.[2,19] The infrared absorption (from ~750 nm to over 1500 nm) can be attributed to transitions within the IB between Nb t_{2g} states[22,23] and/or may also arise due to plasmonic excitation.[23,24] Transitions within the IB are metallic in character and can occur at a broad range of energies. However, these types of transitions most likely generate carriers that are difficult to separate and instead rapidly recombine.

The optoelectronic properties of strontium niobate can also be modified by doping enabling a high degree of tunability.[25] The energy gap has also been demonstrated to be tunable by Sr content and ranges from 1.82 eV to 1.85 eV for $x = 0.8$ and $x = 0.9$ respectively, whilst for $x \geq 0.92$ there is an increase in energy gap towards ~1.9 eV.[19] Overall, these reports indicate strongly that an Sr fraction of 0.9 is the ideal starting point for studying other applications that wants to take advantage of the material's opto-electronic properties.

One of the most significant challenges surrounding strontium niobate relates to its high temperature synthesis conditions, which allow little flexibility in the fabrication of application devices. This presents some fabrication challenges for devices based on a thin film such as solar cells, which have probably discouraged or hindered successful implementation in many applications.

We first overcome the immense challenge associated with the deposition of an extremely thin absorber layer of metal oxide particles. We demonstrate nanoparticulate film formation from metallic, air-stable, non-toxic cubic perovskite oxide strontium niobate with the chemical formula $Sr_{0.9}NbO_3$. After femtosecond (fs) laser treatment to fragment $Sr_{0.9}NbO_3$ without varying its composition, the film was deposited using a vacuum glancing angle aerosol spray technique. With a successful absorber layer fabrication process, our film-based test structures have shown, for the first time, carrier separation and extraction from a metal-like oxide. These findings could open up great opportunities to harvest a very broad solar spectral absorption range with reduced recombination losses. Our results not only encourage further investigations on strontium niobate but should also inspire the development and study of materials which could exhibit a similar electronic structure.

2. Results and discussion

2.1 Material composition

The composition $Sr_{0.9}NbO_3$ was selected for investigation due to it having the greatest photocatalytic performance of the series studied by Xu *et al.*[2] and Efstathiou *et al.*[19] whilst ensuring the cubic perovskite phase and smaller energy gap. $Sr_{0.9}NbO_3$ was synthesised by calcination as previously reported.[2] Our investigations and previous attempts to fabricate thin films suitable test structures based on un-fragmented and/or milled/crushed $Sr_{0.9}NbO_3$ were unsuccessful due to the large particle size (200 nm to 2 μm diameter on average) which led to inhomogeneous and rough film formation. We therefore employed a laser fragmentation technique. In order to facilitate film fabrication at low temperature, we have fragmented the large crystals into smaller colloidal particles (<50 nm) by fs-laser processing in liquid.[26] A glancing angle spray deposition technique was then employed to ensure that the remaining larger particles are deflected and do not adhere to the substrate (see ESI, Fig. S1†).

2.2 Materials characterisation

We first confirmed that there were no structural or chemical changes to $Sr_{0.9}NbO_3$ following laser fragmentation by using transmission electron microscopy (TEM) X-ray diffraction

(XRD), X-ray photoelectron spectroscopy (XPS) and ultraviolet-visible (UV-vis) absorption measurements. The TEM images for as-prepared and fragmented $Sr_{0.9}NbO_3$ are presented in Fig. 2. TEM images for as-prepared $Sr_{0.9}NbO_3$ are shown in Fig. 2a and b and for laser-fragmented $Sr_{0.9}NbO_3$ are shown in Fig. 2d–e. Typically, we observe that the laser fragmentation leads to the formation of more dispersed and smaller spherical particles (Fig. 2d–e). The formation of smaller and spherical particles is favourable for film fabrication due to improved packing of nanoparticles. In order to study further any crystallographic changes following laser fragmentation, the selected area electron diffraction (SAED) patterns are shown in Fig. 2c, as-prepared, and Fig. 2f, laser-fragmented, which correspond to the area shown in the TEM images in Fig. 2a and d respectively. The SAED pattern for the as-prepared $Sr_{0.9}NbO_3$ sample indicates crystalline phases. The SAED pattern for laser-fragmented $Sr_{0.9}NbO_3$ present fewer spots in the ring arrangements due to the particles being more dispersed. Comparing the positions of the ring and bright spots, we observe that the *d*-spacing for the as-prepared and laser-fragmented samples are the same. The first plane (110) is well defined in the SAED pattern for both samples and is also the most intense peak observed in the XRD spectra (Fig. 2g).

The XRD pattern for the as-prepared and fragmented $Sr_{0.9}NbO_3$ is shown in Fig. 2g. The main peaks for both the as-prepared sample and the laser-fragmented sample occur at the same positions and agree with the literature for $Sr_{0.9}NbO_3$ powder previously reported[2,19] and indicates that there are no crystallographic changes to $Sr_{0.9}NbO_3$ following laser fragmentation. There was no change in the full width at half-maximum (FWHM) and the relative peak intensity was similar for both samples.

We also observe no changes in the X-ray photoelectron spectroscopy (XPS) spectra for as-prepared and laser fragmented $Sr_{0.9}NbO_3$, indicating that the chemical composition is unchanged following laser-fragmentation (Fig. 3a, b and c). We present data for the Nb 3d peak, which provides information on the oxidation state of Nb. The average valence of Nb in $Sr_{0.9}NbO_3$ is expected to be +4.4[20,21] and therefore the Nb 3d doublet in $Sr_{0.9}NbO_3$ is a convolution of the Nb^{4+} and Nb^{5+} 3d doublets. We observe that the valence is between 4+ and 5+ for all samples confirming that the material is not oxidised following the fs laser treatment. We also calculated that the ratio between the 4+ and 5+ peaks remained similar after laser fragmentation and was between 2.8–3 : 1. The XPS spectra for the O 1s peak is shown in Fig. 3c and confirms there were no major changes. Since there was not a significant change in the binding energies between the as-prepared and laser fragmented samples and the ratios between Nb 4+ and 5+ remained similar, it is confirmed that laser fragmentation does not change the chemical structure of the material, which is also supported by TEM, XRD and optical measurements.

The UV-vis absorption spectra for as-prepared and laser-fragmented $Sr_{0.9}NbO_3$ is shown in Fig. 3d. Both samples display broad absorption (see transmittance in the inset of Fig. 3d) in the visible spectrum continuing into the near-infrared (NIR), in agreement with the results published on stoichiometric strontium niobate ($SrNbO_3$)[27] and with minor differences before and after fragmentation, mainly due to differing concentrations between samples. Tauc plots for as-prepared

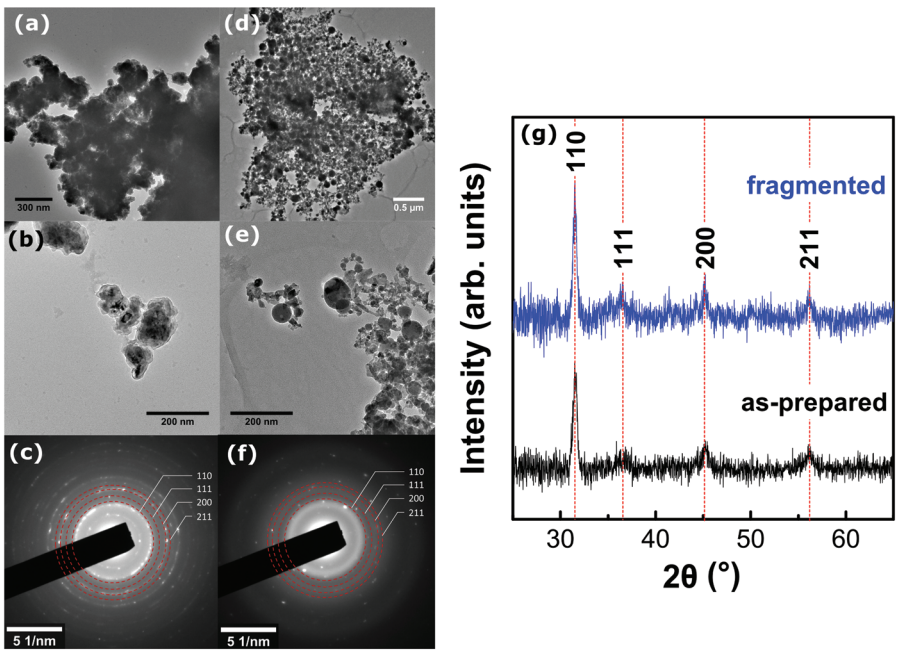

Fig. 2 Transmission electron microscopy images and selected area electron diffraction (SAED) patterns of $Sr_{0.9}NbO_3$ before (a–c) and after (d–f) laser fragmentation. The SAED patterns shown in (c) and (f) correspond to the area shown in (a) and (d) respectively. (g) X-ray diffraction scan of drop-casted $Sr_{0.9}NbO_3$ nanoparticles before (black) and after (blue) laser fragmentation.

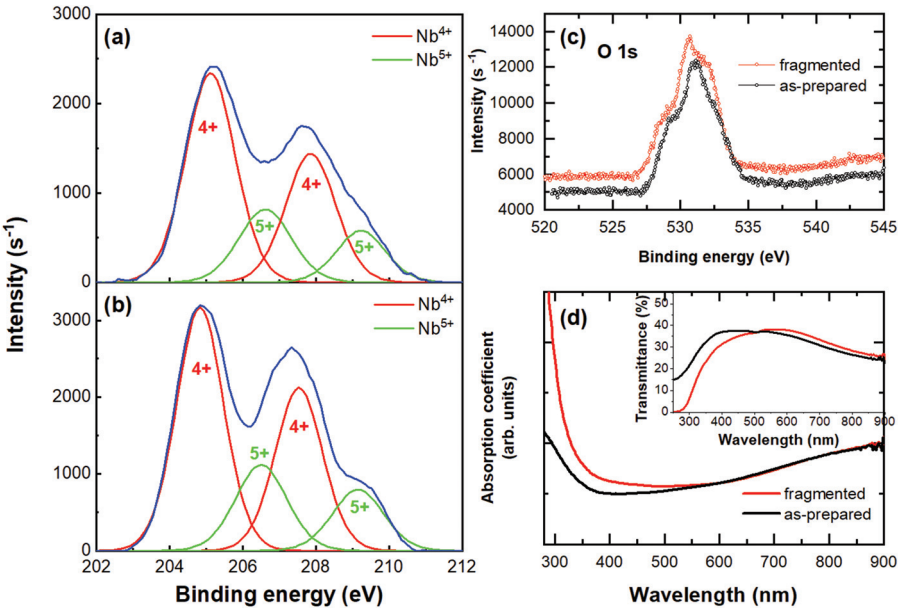

Fig. 3 X-ray photoelectron spectroscopy (XPS) spectra and ultraviolet-visible (UV-vis) absorption spectra for $Sr_{0.9}NbO_3$. (a) XPS spectra for as-prepared $Sr_{0.9}NbO_3$ and (b) XPS spectra for fs laser fragmented $Sr_{0.9}NbO_3$ for the Nb 3d doublet. The binding energies were referenced to the adventitious C 1s peak (284.6 eV). (c). X-ray photoelectron spectra for O 1s peak indicating no change after laser fragmentation. (d) UV-vis absorption coefficient for as-prepared and fragmented $Sr_{0.9}NbO_3$ nanoparticles, prepared by drop-casting on quartz. The inset shows the corresponding transmittance (%).

and laser-fragmented $Sr_{0.9}NbO_3$ are shown in Fig. S3 (ESI†) and indicate an energy gap of approximately 2.1 eV.

2.3 Film formation and carrier extraction measurements

Test structures that included $Sr_{0.9}NbO_3$ nanoparticles films were fabricated to verify the possibility of extracting photo-generated carriers; these were fabricated with glass/indium-doped tin-oxide(ITO)/compact-TiO_2/mesoporous-TiO_2/$Sr_{0.9}NbO_3$/spiro-OMeTAD/Ag. These test structures closely resemble that of photovoltaic devices because it was important to work with well-known and tested fabrication methods and materials so to minimize unknown phenomena and to aid the analysis of the results. The test structure is shown schematically in Fig. 4a and the energy band diagram is shown in Fig. 4b. The Fermi level of $Sr_{0.9}NbO_3$ was determined by Kelvin probe measurements (see Fig. S4, ESI†) and was measured to be −5.2 eV relative to the vacuum level. The energy band positions of TiO_2 and spiro-MeOTAD are based on those reported in the literature.[28,29] Details of the fabrication steps can be found in the experimental details section.

We successfully fabricated test structures using $Sr_{0.9}NbO_3$, which clearly demonstrate the possibility of carrier extraction (Fig. 4c and d). The forward and reverse current density–voltage (J–V) characteristic for the test structure with the best results is shown in Fig. 4c. Measurements were taken in the range of −0.1 V to 0.6 V, and 'forward' refers to a scan direction from negative to positive bias and 'reverse' refers to a scan direction from positive to negative bias. We measure an appreciable current density at short-circuit conditions of 0.273 mA cm^{-2} (0.270 mA cm^{-2} in reverse sweep), which demonstrates the possibility of carrier extraction. Although our main goal is to analyse the possibility of carrier extraction, for information we can also report other parameters in forward (reverse) bias that relate to the photovoltaic operation of this test structure and that demonstrate Fermi level splitting and the generation of a photovoltage: short-circuit current density (J_{SC}) of 0.273 mA cm^{-2} (0.270 mA cm^{-2}), open-circuit voltage (V_{OC}) of 452 mV (452 mV), fill factor (FF) of 26% (29%) and an overall power conversion efficiency (PCE) of 0.032% (0.035%). It is expected that carrier extraction is possible due to the extremely thin absorber layer of $Sr_{0.9}NbO_3$ which enables the transport of carriers to the transport layers. Whilst the test structure exhibits overall limited performance as an actual solar cell device and device optimization will be required, here we use these results to demonstrate that it is possible to separate carriers generated in metallic $Sr_{0.9}NbO_3$ leading to a photocurrent. We will argue and show further below that the origin of carrier separation in $Sr_{0.9}NbO_3$ is due to Nb 4d–Sr 3d interband transitions and weak Nb 4d–Nb 4d intraband transitions, and/or a possible contribution from plasmonic absorption, which was previously reported in the literature.[23,24] However, the analysis of the parameters can here be useful to analyse the transport mechanisms.

The devices showed very little J–V hysteresis in the forward and reverse scans (Fig. 4c); however, it was typically observed that a scan in the reverse direction gave a marginally higher fill factor. Despite this, there were no changes in the V_{OC} and negligible change in the J_{SC} when the scan direction was reversed. The J–V curves at different scan rates (150, 300, 750 and 1500 mV s^{-1}) is shown in Fig. S5 (ESI†) and we observed

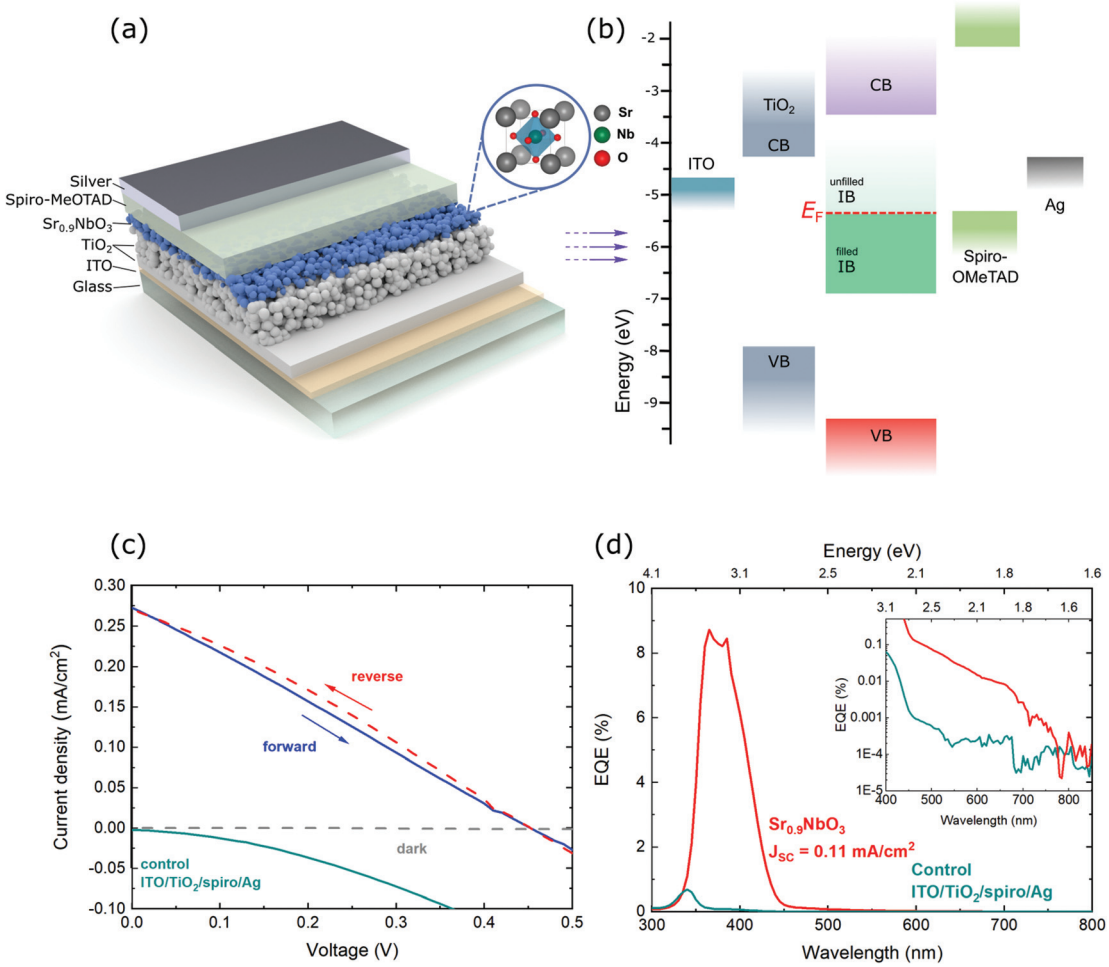

Fig. 4 (a) Schematic of the $Sr_{0.9}NbO_3$ test device structure used to demonstrate carrier extraction and (b) energy band alignment. (c) Current density–voltage (J–V) characteristic of $Sr_{0.9}NbO_3$ nanoparticle devices in the forward and reverse sweep direction. Included is the J–V for a solar cell fabricated with absence of $Sr_{0.9}NbO_3$ nanoparticles, confirming the photocurrent originates from the perovskite. (d) External quantum efficiency (EQE) for the corresponding $Sr_{0.9}NbO_3$ solar cell device, including the control device EQE. The inset shows the same data from the red curve with truncated y-axis to indicate the photocurrent onset.

no change in the test structure parameters for a change in scan rate, indicating that Sr/O vacancies are not migrating under applied bias, whilst the photocurrent observed is not due to a polarization effect.

Fig. 4d shows the external quantum efficiency (EQE) for the corresponding test structure, and the inset of Fig. 4d shows a zoomed-in section of the device EQE curve. We observe a strong photocurrent on-set at approximately 2 eV, which likely corresponds to the indirect energy gap between IB and CB. The EQE for the control without $Sr_{0.9}NbO_3$ nanoparticles, *i.e.* ITO/TiO_2/spiro-OMeTAD/Ag, is also shown to confirm that the photocurrent is generated by the $Sr_{0.9}NbO_3$ nanoparticles.

The majority of the photocurrent was observed at energies >2 eV. Nonetheless, we were still able to collect sub-bandgap energies in the IR range. We observe non-negligible photocurrent in the EQE spectra at energies below the energy gap (at energies as low as ~1.6 eV, corresponding to ~750 nm), shown in the inset of Fig. 4d. Given that the bandgap is 2.1 eV, the origin of sub-bandgap photocurrent is expected to be due to various possible intraband transitions within the IB as reported by Song *et al.*[23] and/or could be due to plasmonic excitations as these have been previously reported.[23,24]. We will discuss the nature of such transitions in the following section of the paper and we can provide further and more specific details on the nature of these transitions.

Fig. 5 shows an annotated band structure of $Sr_{0.9}NbO_3$ and represents the expected transitions in $Sr_{0.9}NbO_3$. The Fermi level has been set to the value measured by Kelvin probe (see Fig. S4, ESI†). Carriers generated due to the absorption of photons with energies greater than the bandgap (2.1 eV) are interband transitions and are excited into the CB of $Sr_{0.9}NbO_3$. These carriers are excited *via* direct (red arrows labelled 1-d) and indirect transitions (red arrows labelled 1-i) and can inject directly into the TiO_2 transport layer.

Transitions represented by black arrows (2) are intraband transitions within the intermediate band. These transitions

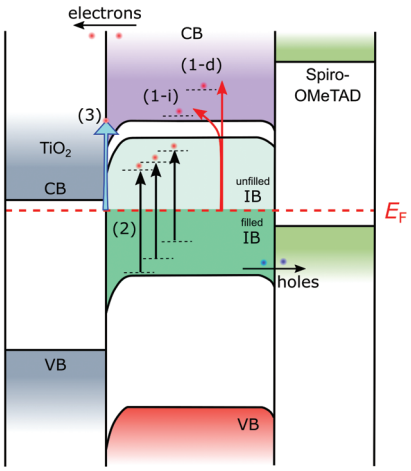

Fig. 5 Fermi-level equilibrated band structure of the $Sr_{0.9}NbO_3$ solar cell displaying the various transitions which may take place in $Sr_{0.9}NbO_3$ leading to a photocurrent.

originate from electrons in the intermediate band and transit to a higher unoccupied state above the Fermi-level. Such excited carriers can inject into the CB of TiO_2 provided that they have sufficient energy. The IB is mostly comprised of Nb t_{2g} orbitals, and transitions between Nb t_{2g} orbitals within the IB are expected to be suppressed due to electron dipole selection rule[22] which likely results in the small photocurrents we observe here, corroborating with previous combined experimental and theoretical results.[23] Although very low, the IB carrier extraction observed here is significant because it demonstrates the possibility of extracting simultaneously carriers resulting from band-to-band transition, which are typical of a semiconductor, as well as carriers excited in a metallic-like band structure. Furthermore, we expect that the prospective goal of achieving higher efficiency in carrier extraction will be possible through the design of suitable and targeted device architectures that will allow to more efficiently utilise excitations in $Sr_{0.9}NbO_3$: both within the IB and from the IB to the CB.

Finally, as plasmonic absorption has previously been reported for differing stoichiometries of $Sr_xNbO_{3+\delta}$[23,24] we should mention the possibility of plasmonic effects, represented here by the blue arrow (3) in Fig. 5. Plasmonic excitations to energies above the TiO_2 CB level can potentially inject into the TiO_2 CB and be extracted. However, we need to stress that this remains an exciting but unproven possibility as it is unlikely that in the current test structure, we are able to extract a meaningful plasmonic current.

3. Summary

We have explored carrier generation and extraction from a metallic oxide perovskite. A test structure using metallic $Sr_{0.9}NbO_3$ perovskite oxide nanoparticles is presented for the first time. Incorporating $Sr_{0.9}NbO_3$ nanoparticles into the test structures without causing shunting is of paramount interest, and was achieved through the fs-laser fragmentation followed by a continuous aerosol spray technique at a glancing angle to deposit nanoparticles of $Sr_{0.9}NbO_3$ as a thin-film, whilst avoiding the deposition of large particles. This allowed for the successful fabrication of test structures without shunting and highlighting intriguing opportunities offered by this type of material.

In particular, we were able to demonstrate simultaneous carrier extraction following band-to-band transition, as typical of a semiconductor, as well as extraction of carriers generated within a metal-like energy band. In the first case, photocurrent generation in this low-energy gap oxide is facilitated by the carrier's spatial separation in the Nb 4d t_{2g} lower states and the Sr 3d higher states; this may provide for segregated carrier transport channels, which reduces recombination probability. Secondly, while the photocurrent generated from NIR absorption is relatively low, we foresee that by optimizing the front selective contact, the possibility exists to harness NIR light through extraction of intra-band excited states close to the junction. This will provide insights to determine if the contacts are sufficiently selective to extract efficiently the photogenerated charges. Further work on the carrier recombination kinetics can also reveal limiting factors for future application devices performance as well as to identify where recombination occurs. We expect that strontium niobate electronic structure, which merges metallic and semiconducting properties, could be possible in a range of similar materials. This opens up the possibility of extensive research in creating optimal electronic configurations for highly efficient solar energy harvesting. Improvements in device fabrication and architecture will necessarily provide the opportunity for higher efficiency in devices with $Sr_{0.9}NbO_3$, and other materials alike preserving good stability and negligible hysteresis. Our results are therefore highly promising in bringing together for the first time, within the same material, beneficial carrier extraction features due to both semiconducting as well as metallic behaviour.

4. Experimental details

Synthesis and fs-laser fragmentation

Strontium niobate $Sr_{0.9}NbO_3$ was synthesised by calcination of homogenized $Sr_4Nb_2O_9$, Nb and Nb_2O_5 mixtures in a flowing Ar atmosphere at 1400 °C for 20 h. The $Sr_{0.9}NbO_3$ pellet obtained following calcination was grinded into a powder and was then ball-milled to further reduce the particle size. Full synthesis details and ball-milling technique are reported elsewhere.[2] The milled powder was then suspended and fragmented by fs pulsed laser in DI water.

For $Sr_{0.9}NbO_3$ fragmentation in water, a fs pulsed laser was used (wavelength 400 nm and pulse width 100 fs) whereby barium borate (BBO) crystal was used to select 400 nm. A schematic diagram and photographs of the laser-fragmentation process are shown in Fig. S2 (ESI†). In particular, in order to achieve efficient fragmentation, we fragmented 5 mg of $Sr_{0.9}NbO_3$ in 5 mL DI water. During irradiation the glass con-

tainer was rotated. The process was conducted at room temperature and for 30 min. The laser beam was shaped and focused onto a spot (2 mm in diameter) on the liquid surface by an optical lens with a focal length of 250 mm. The average laser power was set to be approximately 30 mW while using a repetition rate of 1 kHz.

Characterisation

Samples, before and after fragmentation, were prepared for UV-visible absorption, XRD analysis by drop casting a solution of $Sr_{0.9}NbO_3$ in DI water onto quartz glass. UV-visible absorption measurements were carried out using a PerkinElmer Lambda 650 with a 150 mm integrating sphere. XRD analysis was carried out using a Bruker D8 Discover, using Cu Kα X-rays with wavelength 1.54 Å. Samples were prepared for TEM by drop casting a solution of $Sr_{0.9}NbO_3$ in DI water onto a holey carbon grid. TEM was carried out using a JEOL JEM-2100F. Samples were prepared for XPS by drop casting the same solution onto molybdenum foil. XPS was performed using a Kratos Axis Ultra DLD photoelectron spectrometer with monochromatic Al Kα X-ray radiation. Current and voltage were 10 mA and 15 kV, respectively, at an operating pressure of 10^{-9} bar. The binding energies were referenced to the adventitious C 1s peak (284.6 eV). Fermi level measurements were performed by the Kelvin probe technique (SKP Kelvin probe 4.5, KP Technology Ltd, UK). An Au probe was used as the reference probe (2 mm tip diameter) and the measurement was performed in ambient conditions. Prior to the sample measurement, the system was calibrated using an Au reference sample provided by KP Technology with a known work function of 5.1 eV. Samples were prepared by depositing $Sr_{0.9}NbO_3$ onto Au-coated glass. Au-coated glass was first prepared by sputter deposition of a thick layer of gold to cover the entire surface of the glass. $Sr_{0.9}NbO_3$ was then deposited *via* spray coating a solution of $Sr_{0.9}NbO_3$ in ethanol through a mask such that only half of the Au-coated glass was covered (see Fig. S4, ESI†). The Au-coated glass substrate was heated to 100 °C during deposition. The probe was scanned across an interface between the sample and the Au-coated glass substrate. All measurements were performed at room temperature and in ambient conditions.

Fabrication of solar cell devices

ITO-patterned glass was cleaned by O_2 plasma. A TiO_2 compact blocking layer was formed by first preparing a solution of 1.56 mL titanium(IV) isopropoxide and 0.394 g triethanolamine in 18 mL ethanol. The solution was then stirred for 2 hours at 40 °C and then left for 24 hours at room temperature. The solution was then spin-coated at 4000 revolutions per minute (RPM) for 30 seconds and then annealed at 400 °C in a furnace for 2 hours. The mesoporous TiO_2 layer was deposited by spin-coating (2000 RPM for 60 seconds) a solution of commercial dyesol 18-NRT titania nanoparticle paste dissolved in ethanol in a 1 : 2 ratio of paste to ethanol. The films were then annealed in a furnace at 400 °C for 2 hours.

For the fabrication of solar cell devices, laser-fragmented $Sr_{0.9}NbO_3$ was deposited from suspension in DI water and under vacuum by spray coating. Spray coating was performed at a glancing angle as previously reported[30] in order to ensure that a uniform film was deposited which resulted in the deposition of the smallest particles. A schematic diagram and photographs of the glancing angle spray deposition technique are shown in Fig. S1 (ESI†). In detail, the apparatus consisted of a colloidal solution tank, stopper valve (V) placed after the tank and a spray nozzle. The IOTA ONE (Parker) valve driver for high speed solenoid valves was used to control automatically the duration range of the valve. The solution was prepared by fs-laser treatment as described previously without any additional filtration. The colloidal solution was poured into a glass beaker. The synchronized stopper valves help to perform pulsed deposition by a stop or start action with any desired time interval. The pulse duration for the valve was 0.5 s open and 1 s closed, which was repeated 30 times until 10 mL $Sr_{0.9}NbO_3$ colloidal solution was used. For this experiment, we used a 5 mg/5 mL water solution twice. During deposition, the pressure in chamber decreased from 2×10^{-5} Torr to 10^{-2} Torr. The substrate was rotated during deposition, and the spray was pulsed. The thickness of the film was approximately 50 nm, determined by atomic force microscopy; however, due to the roughness and porosity of the mesoporous TiO_2 underlayer, the film presented large variations.

The hole transport layer was prepared by dissolving 0.207 g Spiro-MeOTAD in 1.00 mL chlorobenzene and deposited by spin-coating at 3000 RPM for 30 seconds. Providing that the spiro-OMeTAD layer is sufficiently thick, it ensured that the perovskite is completely covered and not exposed to the metal top contacts. Silver metal contacts were deposited by thermal evaporation using a shadow mask. The resulting active area of the device was 0.04 cm^2.

Solar cell test devices characterization

Normalized solar spectrum AM1.5G was generated using Wacom Electric Co. solar simulator (JIS, IEC standard conforming, CLASS AAA) calibrated to give 100 mW cm^{-2} using an amorphous silicon (a-Si) reference cell. The electrical data was recorded using a Keithley 2400 source meter. Devices were measured in the voltage range −0.1 V to 0.6 V without any voltage pre-conditioning (*i.e.* without voltage soaking). The solar cells were light-soaked for 3 min prior to measurement to allow the *J–V* character to stabilise. The scan rate used was between 150 mV s^{-1} and 1500 mV s^{-1} and was varied by altering the full *J–V* curve acquisition time, whilst each current point acquisition at a specific applied voltage remained constant for all measurements. This was achieved by altering the voltage step size and the number of points measured between a fixed voltage range, which ensures that each data point is measured under the same conditions. The number of power line cycles (NPLC), *i.e.* the number of times the input signal is integrated to obtain a single measurement, was set to 10 cycles and the delay time, *i.e.* the delay between applying the voltage and the measurement of the signal, was set to 5 ms. The NPLC

and the delay time remained constant for all measurements. All devices were tested in air and at room temperature. The solar cell EQE characteristics were measured in direct current (DC) mode using a 150 W Xenon lamp with monochromator and the spectral response was calibrated using an a-Si reference cell. The step size was 5 nm.

Conflicts of interest

The authors declare no competing interests.

Acknowledgements

This work was supported by EPSRC (EP/K022237/1, EP/M024938/1 and EP/R023638/1), the EPSRC Supergen SuperSolar Hub, the Department for Employment and Learning (DEL) of Northern Ireland Studentship, and by the New Energy and Industrial Technology Development Organization (NEDO).

References

1 C. Ng, J. J. Cadusch, S. Dligatch, A. Roberts, T. J. Davis, P. Mulvaney and D. E. Gómez, *ACS Nano*, 2016, **10**, 4704–4711.
2 X. Xu, C. Randorn, P. Efstathiou and J. T. S. Irvine, *Nat. Mater.*, 2012, **11**, 595–598.
3 B. A. Apgar, S. Lee, L. E. Schroeder and L. W. Martin, *Adv. Mater.*, 2013, **25**, 6201–6206.
4 S. Lee, B. A. Apgar and L. W. Martin, *Adv. Energy Mater.*, 2013, **3**, 1084–1090.
5 W. S. Fann, R. Storz, H. W. K. Tom and J. Bokor, *Phys. Rev. B: Condens. Matter Mater. Phys.*, 1992, **46**, 13592–13595.
6 R. Ramesh and N. A. Spaldin, *Nat. Mater.*, 2007, **6**, 21–29.
7 C. H. Ahn, *Science*, 2004, **303**, 488–491.
8 G. Rijnders and D. H. A. Blank, *Nature*, 2005, **433**, 369–370.
9 C. C. Homes, *Science*, 2001, **293**, 673–676.
10 R. Nechache, C. Harnagea, S. Li, L. Cardenas, W. Huang, J. Chakrabartty and F. Rosei, *Nat. Photonics*, 2014, **9**, 61–67.
11 I. Grinberg, D. V. West, M. Torres, G. Gou, D. M. Stein, L. Wu, G. Chen, E. M. Gallo, A. R. Akbashev, P. K. Davies, J. E. Spanier and A. M. Rappe, *Nature*, 2013, **503**, 509–512.
12 R. J. Cava, B. Batlogg, J. J. Krajewski, R. Farrow, L. W. Rupp, A. E. White, K. Short, W. F. Peck and T. Kometani, *Nature*, 1988, **332**, 814–816.
13 J. Zhu, H. Li, L. Zhong, P. Xiao, X. Xu, X. Yang, Z. Zhao and J. Li, *ACS Catal.*, 2014, **4**, 2917–2940.
14 G. Zhang, G. Liu, L. Wang and J. T. S. Irvine, *Chem. Soc. Rev.*, 2016, **45**, 5951–5984.
15 G. V. Naik, V. M. Shalaev and A. Boltasseva, *Adv. Mater.*, 2013, **25**, 3264–3294.
16 J. Kim, X. Yin, K. C. Tsao, S. Fang and H. Yang, *J. Am. Chem. Soc.*, 2014, **136**, 14646–14649.
17 M. A. Peña and J. L. G. Fierro, *Chem. Rev.*, 2001, **101**, 1981–2018.
18 Z. Fan, K. Sun and J. Wang, *J. Mater. Chem. A*, 2015, **3**, 18809–18828.
19 P. Efstathiou, X. Xu, H. Ménard and J. T. S. Irvine, *Dalton Trans.*, 2013, **42**, 7880–7887.
20 B. Hessen, S. A. Sunshine, T. Siegrist and R. Jimenez, *Mater. Res. Bull.*, 1991, **26**, 85–90.
21 K. Isawa, J. Sugiyama, K. Matsuura, A. Nozaki and H. Yamauchi, *Phys. Rev. B: Condens. Matter Mater. Phys.*, 1993, **47**, 2849–2853.
22 Y. Zhu, Y. Dai, K. Lai, Z. Li and B. Huang, *J. Phys. Chem. C*, 2013, **117**, 5593–5598.
23 D. Song, D. Wan, H. H. Wu, D. Xue, S. Ning, M. Wu, T. Venkatesan and S. J. Pennycook, *Nanoscale*, 2020, **12**, 6844–6851.
24 D. Y. Wan, Y. L. Zhao, Y. Cai, T. C. Asmara, Z. Huang, J. Q. Chen, J. Hong, S. M. Yin, C. T. Nelson, M. R. Motapothula, B. X. Yan, D. Xiang, X. Chi, H. Zheng, W. Chen, R. Xu, A. Ariando, A. Rusydi, A. M. Minor, M. B. H. Breese, M. Sherburne, M. Asta, Q. H. Xu and T. Venkatesan, *Nat. Commun.*, 2017, **8**, 15070.
25 C. Sun and D. J. Searles, *J. Phys. Chem. C*, 2014, **118**, 11267–11270.
26 V. Svrcek, D. Mariotti, U. Cvelbar, G. Filipič, M. Lozac'H, C. McDonald, T. Tayagaki, K. Matsubara, M. Lozac'h, C. McDonald, T. Tayagaki and K. Matsubara, *J. Phys. Chem. C*, 2016, **120**, 18822–18830.
27 D. Oka, Y. Hirose, S. Nakao, T. Fukumura and T. Hasegawa, *Phys. Rev. B: Condens. Matter Mater. Phys.*, 2015, **92**, 205102.
28 X.-X. Gao, Q.-Q. Ge, D.-J. Xue, J. Ding, J.-Y. Ma, Y.-X. Chen, B. Zhang, Y. Feng, L.-J. Wan and J.-S. Hu, *Nanoscale*, 2016, **8**, 16881–16885.
29 Z. Hawash, L. K. Ono and Y. Qi, *Adv. Mater. Interfaces*, 2018, **5**, 1700623.
30 V. Švrček, C. McDonald, M. Lozac'h, T. Tayagaki, T. Koganezawa, T. Miyadera, D. Mariotti and K. Matsubara, *Energy Sci. Eng.*, 2017, **5**, 184–193.